

## SPECTROSCOPIC EVIDENCE OF ALFVÉN WAVE DAMPING IN THE OFF-LIMB SOLAR CORONA

G. R. GUPTA

Inter-University Centre for Astronomy and Astrophysics, Post Bag-4, Ganeshkhind, Pune 411007, India  
*Draft version August 12, 2021*

### ABSTRACT

We investigate off-limb active region and quiet Sun corona using spectroscopic data. Active region is clearly visible in several spectral lines formed in the temperature range of 1.1–2.8 MK. We derive electron number density using line ratio method, and non-thermal velocity in the off-limb region up to the distance of 140 Mm. We compare density scale heights derived from several spectral line pairs with expected scale heights as per hydrostatic equilibrium model. Using several isolated and unblended spectral line profiles, we estimate non-thermal velocities in active region and quiet Sun. Non-thermal velocities obtained from warm lines in active region first show increase and later show either decrease or almost constant value with height in the far off-limb region, whereas hot lines show consistent decrease. However, in the quiet Sun region, non-thermal velocities obtained from various spectral lines show either gradual decrease or remain almost constant with height. Using these obtained parameters, we further calculate Alfvén wave energy flux in the both active and quiet Sun regions. We find significant decrease in wave energy fluxes with height, and hence provide evidence of Alfvén wave damping. Furthermore, we derive damping lengths of Alfvén waves in the both regions and find them to be in the range of 25-170 Mm. Different damping lengths obtained at different temperatures may be explained as either possible temperature dependent damping or measurements obtained in different coronal structures formed at different temperatures along the line-of-sight. Temperature dependent damping may suggest some role of thermal conduction in the damping of Alfvén waves in the lower corona.

*Keywords:* Sun: Corona — Sun: UV radiation — Waves — Turbulence

### 1. INTRODUCTION

Heating of solar atmosphere and acceleration of solar wind remain two of the most puzzling problems in the solar and space physics. There are several theories proposed to explain the phenomena, however, to identify any one dominant process is extremely difficult to do. For details, see [Parnell & De Moortel \(2012\)](#), and [De Moortel & Browning \(2015\)](#) and references therein for current progress in the field. Most of the models proposed so far are attributed to either dissipation of magnetohydrodynamics (MHD) waves or magnetic reconnection. Among the several proposed ideas, role of wave turbulence in the heating of solar corona and acceleration of solar wind is one of the well studied model (see recent reviews by [Arregui 2015](#); [Cranmer et al. 2015](#)). [Alfvén \(1942\)](#) first suggested existence of electromagnetic-hydrodynamic waves in the solar atmosphere and its importance in the heating of solar corona ([Alfvén 1947](#)). This led to the wave heating model of solar corona. In this model, convective motions at the footpoints of magnetic flux tubes are assumed to generate wave-like fluctuations that propagate up into the extended corona ([Cranmer & van Ballegoijen 2005](#); [Suzuki & Inutsuka 2005](#)). These fluctuations are often proposed to partially reflect back down toward the Sun, develop into strong magnetohydrodynamics (MHD) turbulence, and dissipate gradually ([Cranmer et al. 2007](#); [Verdini et al. 2010](#)). Recently, [Van Ballegoijen et al. \(2011\)](#) developed a three-dimensional magnetohydrodynamics (MHD) Alfvén wave turbulence model to explain the heating of both solar chromosphere and corona in the coronal loop. Another model used to explain coronal heating is nanoflare heating model (see recent review by [Klimchuk 2015](#)). In this model, random photospheric motions and flows lead to twisting and braiding of coronal field lines. This results in building up of magnetic stress, and thus, leads to re-

lease of energy in the form of impulsive heating events called as nanoflares ([Parker 1988](#)).

In order to understand wave heating mechanism of solar atmosphere, observations of detection, propagation, and dissipation of waves are essential. [Tomczyk et al. \(2007\)](#) and [McIntosh et al. \(2011\)](#) reported the ubiquitous presence of outward propagating Alfvénic (transverse) waves in the solar corona. Propagating Alfvénic waves were also found in the polar region ([Gupta et al. 2010](#); [Morton et al. 2015](#)). Comprehensive review exists on the detection of propagating waves in the solar atmosphere, e.g., [Banerjee et al. \(2011\)](#); [De Moortel & Nakariakov \(2012\)](#); [Jess et al. \(2015\)](#). In recent studies, evidence of damping of propagating waves are also reported ([Morton et al. 2014](#); [Gupta 2014](#); [Krishna Prasad et al. 2014](#)). Signatures of Alfvén waves can also be found through the study of broadening of spectral line profiles in the solar corona (e.g., [Banerjee et al. 2009](#); [Jess et al. 2009](#)). Alfvénic wave motions are transverse to the direction of propagation. In case of field lines aligned in the plane of sky, plasma motions due to Alfvénic waves will either be directed towards or away from the line-of-sight. In the off-limb corona, several spatially unresolved structures may be present along the line-of-sight with different phases of oscillations. These unresolved wave motions can lead to non-thermal broadening of spectral line profiles. Thus, observed non-thermal broadening of spectral line profiles in the corona will be proportional to Alfvén wave amplitude, e.g., [Moran \(2001\)](#).

There are numerous studies devoted to measure off-limb non-thermal broadening of spectral lines to search for any wave activity. [Hassler et al. \(1990\)](#) performed the first observations of high temperature line profiles in the solar off-limb region using sounding rocket experiments. They found increase in line width with height above the limb and interpreted as a signature of propagating hydromagnetic waves in the solar corona. Later, more studies were carried out using space

based SUMER instrument on-board SOHO. Using SUMER, Doyle et al. (1998) and Banerjee et al. (1998) found increase in non-thermal line width with off-limb height and associated density decrease. Their results were in excellent agreement with predictions from outward propagating undamped Alfvén waves. Harrison et al. (2002) performed similar analysis on off-limb part of quiet Sun corona using CDS instrument on-board SOHO. They found narrowing of line width with height and interpreted as indication of wave dissipation in a closed loop system in the low corona. Banerjee et al. (2009) performed similar analysis on polar plume and interplume region using Extreme-Ultraviolet Imaging Spectrometer (EIS, Culhane et al. 2007) on-board Hinode (Kosugi et al. 2007). They found signatures of outward propagating undamped linear Alfvén waves within  $1.1 R_{\odot}$ . Recently, Bemporad & Abbo (2012) and Hahn et al. (2012) measured non-thermal line width up to  $1.4 R_{\odot}$  in the open magnetic field of polar regions using EIS/Hinode. They found signature of damping of Alfvén waves beyond  $1.1 - 1.14 R_{\odot}$ . Lee et al. (2014) investigated cool loop and dark lane over a off-limb active region and obtained basic plasma parameters as a function of height above the limb. They found slight decrease in non-thermal velocity along the cool loop whereas sharp fall along the dark lane. They attributed these findings to wave damping. Hahn & Savin (2014) also measured energy and dissipation of Alfvénic waves in the quiet Sun region.

Recently, Van Ballegooijen et al. (2011) developed a 3-D MHD model of Alfvén wave turbulence to explain the heating of solar chromosphere and corona in the coronal loop. This model has attracted lot of attention from the community to look for such signatures (e.g. Asgari-Targhi et al. 2014). In this work, we focus on off-limb active region loop system and quiet Sun corona to study propagation of Alfvén waves with height and search for any signature of their damping over a wide range of temperature. As Alfvén wave energy flux density is given by (e.g. Moran 2001),

$$E_D = \rho \xi^2 V_A = \sqrt{\frac{\rho}{4\pi}} \xi^2 B \quad (1)$$

where  $\rho$  is mass density ( $\rho = m_p N_e$ ,  $m_p$  is proton mass, and  $N_e$  is electron number density),  $\xi$  is Alfvén wave velocity amplitude, and  $V_A$  is Alfvén wave propagation velocity given as  $B/\sqrt{4\pi\rho}$ . Therefore, total wave energy flux crossing a surface area  $A$  will be given by,

$$E_F = \frac{1}{\sqrt{4\pi}} \sqrt{m_p N_e} \xi^2 B A \quad (2)$$

Henceforth, total Alfvén wave energy flux depends on electron number density, wave amplitude, magnetic field, and area of cross section. In this paper, our main focus is to estimate total wave energy flux with height in the off-limb solar corona, and thus, to find any signatures of wave damping. For the purpose, we identified a unique set of good spectroscopic data covering the off-limb active region and quiet Sun observed by EIS/Hinode. Data covers various spectral lines formed over a wide range of temperature. Previous such studies were mainly carried out with few spectral lines formed at very similar temperature e.g. Fe XII, and Fe XIII. Therefore, current study provides an unique opportunity to carry out such analysis for coronal structures formed over a wide range of temperature. This may also enable us to find any possible existence of temperature dependence. Related details of observations are de-

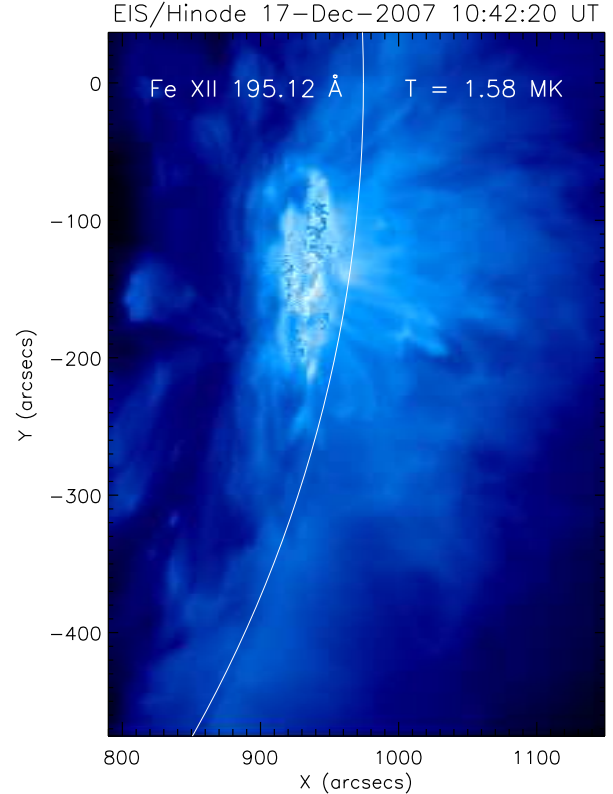


**Figure 1.** Intensity map of off-limb active region and quiet Sun in Fe XII 195.12 Å spectral line rastered by EIS/Hinode on 17 December 2007. Continuous white line indicates location of solar limb.

scribed in § 2. We employ spectroscopic methods to obtain electron number density, and non-thermal velocity which are described in § 3.1, and § 3.2 respectively. In § 3.3, we describe calculation of Alfvén wave energy flux using obtained parameters. Obtained results are discussed in § 4, and final summary and conclusions are provided in § 5.

## 2. OBSERVATIONS AND DATA ANALYSIS

Off-limb active region AR 10978 was observed by EIS/Hinode on 17 December 2007. EIS observations were carried out with  $2''$  slit and exposure time of 45 s. Observations were performed over the wavelength range of 180–204 Å and 248–284 Å. Raster scan started at 10:42:20 UT and completed at 13:02:17 UT and covered a field of view of  $360'' \times 512''$ . This dataset was previously analyzed by O’Dwyer et al. (2011) to study electron density and temperature structure of a limb active region. We followed standard procedures for preparing the EIS data using IDL routine EIS\_PREP<sup>1</sup> available in the *Solar Software* (SSW; Freeland & Handy 1998). Recently, Brooks & Warren (2016) and Testa et al. (2016) showed that absolute calibration of EIS data leads to a systematic overestimation of spectral line widths for most of the pixels along slit. Thus, for the purpose of measuring line widths, we obtained EIS spectra in the data number (DN) unit by applying EIS\_PREP routine with /noabs keyword. Moreover, we also obtained EIS spectra in the physical units ( $\text{erg cm}^{-2} \text{s}^{-1} \text{sr}^{-1}$ ) to further perform electron number density diagnostics. Routine also provides errorbars on the

<sup>1</sup> [ftp://sohoftp.nascom.nasa.gov/solarsoft/hinode/eis/doc/eis\\_notes/01\\_EIS\\_PREP/eis\\_swn](ftp://sohoftp.nascom.nasa.gov/solarsoft/hinode/eis/doc/eis_notes/01_EIS_PREP/eis_swn)

obtained intensities. In addition, there also exists 22% uncertainty in the observed intensity based on pre-flight calibration of EIS (Lang et al. 2006). All the EIS spectral line profiles were fitted with Gaussian function using EIS\_AUTO\_FIT<sup>2</sup>. Routine also provides one-sigma errorbars on the fitted parameters. Comparison between both type of spectra reconfirms the systematic overestimation of line widths from absolutely calibrated data as recently reported by Brooks & Warren (2016) and Testa et al. (2016). However, magnitude of this systematic overestimation of line-widths were found to be very small in the current dataset. As EIS sensitivity is evolving over time, absolutely calibrated data (in physical units) and related errors were further recalibrated using the method of Warren et al. (2014). There exists spatial offsets in the solar-X and solar-Y directions between images obtained from different wavelengths. These offsets were corrected with respect to image obtained from Fe XII 195.12 Å spectral line<sup>3</sup>. Figure 1 shows intensity map of observed off-limb active region obtained from Fe XII 195.12 Å line. Observed active region is very bright and has several saturated image pixels at few locations.

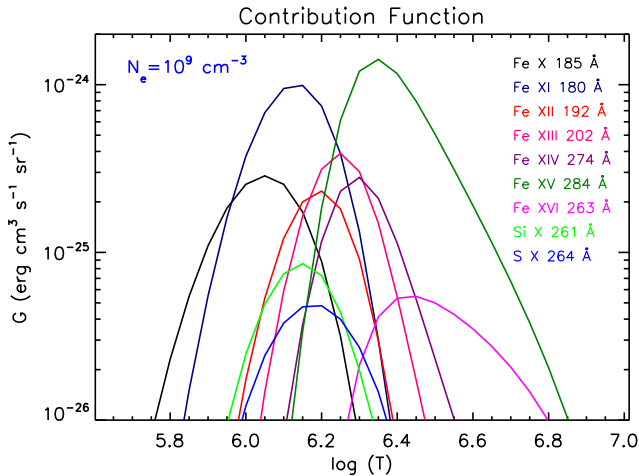


**Figure 2.** Contribution function of spectral lines selected for detailed analysis of off-limb active and quiet Sun regions recorded by EIS/Hinode (see also Table 1).

To identify spectral line wavelengths and corresponding peak formation temperatures, all the atomic data used in this study are taken from CHIANTI atomic database (Dere et al. 1997; Del Zanna et al. 2015). To perform line width analysis, we identified several unblended and isolated spectral lines with good signal strength as highlighted by Young et al. (2007) (see Table 1). Although there exist some blend in Fe XIV 274 Å, and Fe XV 284 Å lines, their contribution can safely be ignored in the active region conditions. Lines are chosen in such a way to get good coverage over temperature range. Contribution function of selected spectral lines were calculated using the CHIANTI v.8 (Del Zanna et al. 2015) at constant electron number density  $N_e = 10^9 \text{ cm}^{-3}$ . Obtained contribution function curves are plotted in Figure 2. Peak formation temperature of all the selected lines are also provided in Table 1. We identify all the spectral lines formed below 2 MK temperature as warm lines whereas those formed above

2 MK as hot lines. We also identified several density sensitive lines and utilized them only for the purpose of deriving electron number density.

**Table 1**

List of emission lines used in the present study. Lines marked with asterisks (\*) are density sensitive lines and used only to calculate electron number densities.

Ion	Wavelength (Å) <sup>a</sup>	T <sub>peak</sub> (MK) <sup>a</sup>
Fe x	184.537	1.12
Fe xi	180.401, 182.167*	1.37
Si x	258.374*, 261.056	1.41
S x	264.231	1.55
Fe xii	192.394, 196.640*	1.58
Fe xiii	196.525*, 202.044	1.78
Fe xiv	264.789*, 274.204 <sup>b</sup>	2.00
Fe xv	284.163 <sup>c</sup>	2.24
Fe xvi	262.976	2.82

<sup>a</sup> Wavelengths and peak formation temperatures are taken from CHIANTI database.

<sup>b</sup> blended with Si VII 274.180 Å.

<sup>c</sup> blended with Al IX 284.042 Å.

In Figure 3, we plot monochromatic intensity maps of off-limb active region obtained from different emission lines formed over temperature range of 1.1 MK to 2.8 MK. Intensity maps clearly show that structures in the active region are not well defined as discrete loop, instead emissions are more likely diffuse in nature without any sharp boundaries. Diffuse emissions observed from active region in Fe x–Fe xvi lines are real. Such diffuse emissions were also highlighted by several authors in the past (e.g., O’Dwyer et al. 2011). Here, we show diffuse nature of active region with several emission lines formed over 1.1 MK to 2.8 MK.

To study variation of several physical parameters with height, we chose several structures and stripes in the off-limb active region and quiet Sun. Although active region is diffuse in nature, we can still identify some bright loop-like structures extending far in to the corona from Fe XII 192.394 Å intensity map. We traced and analyzed several such structures. Here, we present result from one such structure which was traced up to very far off-limb distance. Traced stripe is named as AR1. Furthermore, to get the average behavior of active region, we binned over whole active region data in the solar-Y direction. Similarly, we also binned over small quiet Sun region in the solar-Y direction to study the quiet Sun. Boxes chosen to obtain the average data are labeled as AR2 and QS. We also traced another stripe parallel to AR1 in the quiet Sun region only for the background study purpose. All the chosen stripes and boxes are shown in Figure 3.

As selected spectral lines are isolated and unblended, we fitted all the profiles with single Gaussian function. In Figure 4, we show examples of spectral line profiles and fitted Gaussian. Profiles were obtained at the off-limb distance of 61 Mm along AR1, AR2, and QS. From the plots, it is clear that all the profiles are symmetric and can be well represented by a single Gaussian function.

One of the factor which may affect our analysis would be contamination from instrumental scattered or stray light. Minimum stray light contribution above the dark current is found to be around 2% of the total on-disk counts for that respective

<sup>2</sup> [http://sohoftp.nascom.nasa.gov/solarsoft/hinode/eis/doc/eis\\_notes/16\\_AUTO\\_FIT/eis\\_auto\\_fit.html](http://sohoftp.nascom.nasa.gov/solarsoft/hinode/eis/doc/eis_notes/16_AUTO_FIT/eis_auto_fit.html)

<sup>3</sup> [http://sohoftp.nascom.nasa.gov/solarsoft/hinode/eis/doc/eis\\_notes/03\\_GRATING\\_DETECTOR\\_ID/eis\\_notes\\_03\\_of\\_04.html](http://sohoftp.nascom.nasa.gov/solarsoft/hinode/eis/doc/eis_notes/03_GRATING_DETECTOR_ID/eis_notes_03_of_04.html)

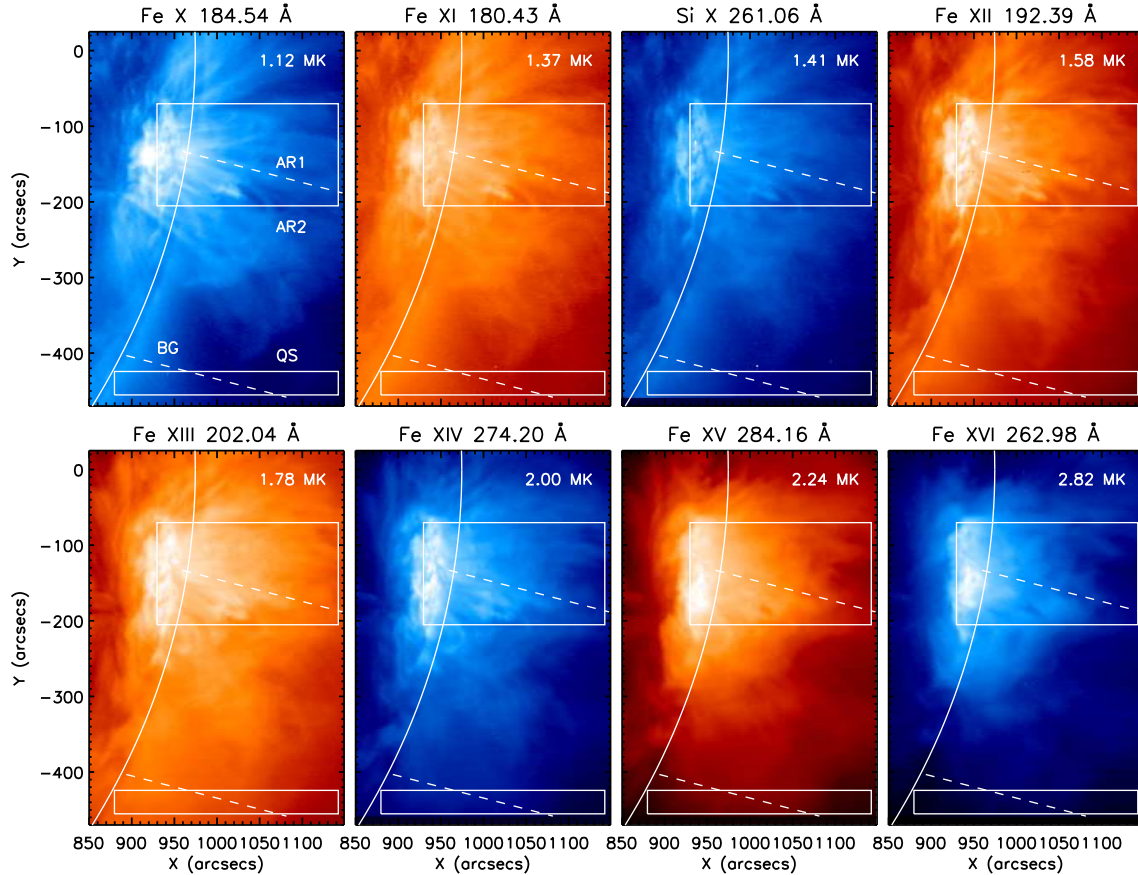


**Figure 3.** Monochromatic intensity maps of off-limb active region and quiet Sun obtained in different wavelengths using EIS/Hinode (as labeled). Dashed white lines on each panel indicate off-limb locations (active region AR1, AR2, and quiet Sun QS) chosen for detailed analysis. Continuous white line on each panel indicates location of solar limb.

line<sup>4</sup>. We chose sufficient box size to calculate average counts from each spectral line in the on-disk part of Sun. As stray light contamination in the off-limb corona will be simply 0.02 times of average counts, we obtained fraction of stray light contribution along all the stripes for all the lines. As intensity drops-off with height in the off-limb corona, stray light contribution increases with height. We found stray light contributions to be less than 8% up to the off-limb distance of  $\approx 140$  Mm along AR1 and AR2 in all the spectral lines except for Fe xvi 263 Å. These contributions were obtained after using 2% weightage of on-disk counts. For Fe xvi 263 Å spectral line, stray light contributions were below 9% up to the distance of 100 Mm. Beyond that distance, contribution increases sharply to about 20% and 35% along AR1 and AR2 respectively. For the quiet Sun region QS, stray light contributions were less than 15% up to very far distance ( $\approx 125$  Mm) in most of the spectral lines. Stray light contributions in Fe x 185 Å, Fe xiv 274 Å, and Fe xv 284 Å lines increase sharply to above 40% for distances beyond 130 Mm, whereas that in Fe xvi 262.976 Å goes beyond 100% for most of the distances along QS. This may indicate that signal in Fe xvi 262.976 Å line along QS is mainly from scattered light. Near the limb, stray light contributions for all the stripes are much smaller ( $< 3\%$  for heights  $< 80$  Mm and  $< 90$  Mm along AR1 and AR2 respectively, whereas  $< 5\%$  for heights  $< 50$  Mm for QS). As noted by [Hahn et al. \(2012\)](#), stray light con-

taminations start affecting line width measurements only if its contributions are more than 45%. In the current analysis, as stray light contributions are found to be very small, thus, its effects are almost insignificant in the line width measurements. Results obtained in the present analysis are mainly derived from heights where stray light contaminations are very small for most of the spectral lines ( $< 8\%$  for distances up to  $\approx 140$  Mm along AR1 and AR2, and  $< 15\%$  for distances up to  $\approx 125$  Mm along QS).

### 3. RESULTS

As per Equation 2, Alfvén wave energy flux is proportional to  $\sqrt{N_e} \xi^2 BA$ . We describe estimation of electron number density and wave velocity amplitude in the following subsections.

#### 3.1. Intensity, Density, and Emission Measure

In Figure 5, we plot variation of intensity obtained from selected spectral lines with height along active region AR1, AR2, and quiet Sun QS. Associated  $1\sigma$  errorbars are also plotted with the data-points. From the plots, it is clear that dataset has good signal strength in all the selected spectral lines in the off-limb region of solar corona. This makes it suitable to estimate electron number density for the calculation of total Alfvén wave energy flux with height.

Electron number densities obtained from various spectral line pairs in the corona can be compared with hydrostatic equilibrium model. This have been done in the past with imaging observations using Transition Region and Coronal Explorer (TRACE; e.g., [Aschwanden et al. 1999](#)), and

<sup>4</sup> [http://sohoftp.nascom.nasa.gov/solarsoft/hinode/eis/doc/eis\\_notes/12\\_STRAY\\_LIGHT\\_INSTRUMENTATION.pdf](http://sohoftp.nascom.nasa.gov/solarsoft/hinode/eis/doc/eis_notes/12_STRAY_LIGHT_INSTRUMENTATION.pdf)

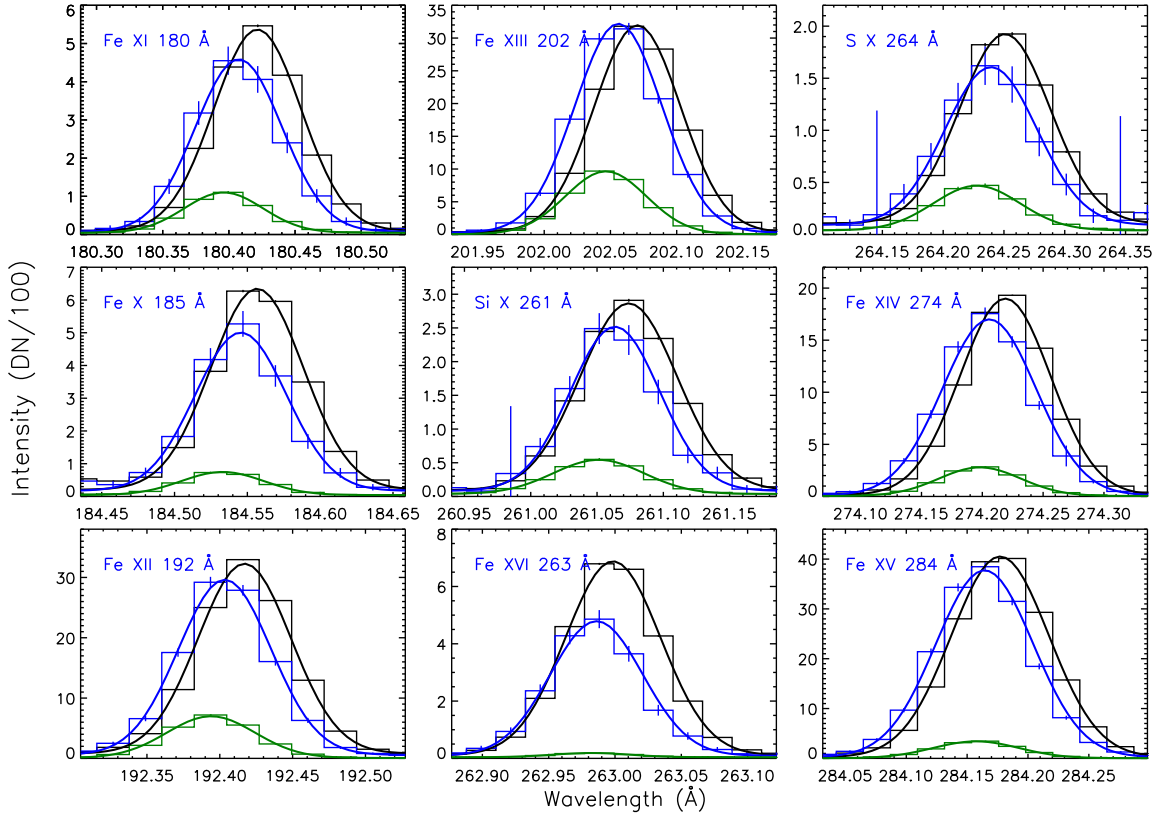


**Figure 4.** Examples of spectral line profiles and fitted Gaussian profiles obtained at the off-limb height of 61 Mm along AR1 (blue lines), AR2 (black lines), and QS (green lines).

recently with spectroscopic observations using EIS/Hinode (e.g., Lee et al. 2014; Gupta et al. 2015).

Electron number density profile in hydrostatic equilibrium is given by,

$$N_e(h) = N_e(0) \exp\left(-\frac{h}{\lambda(T_e)}\right) \quad (3)$$

where  $\lambda$  is density scale height given by,

$$\lambda(T_e) = \frac{2k_b T_e}{\mu m_H g} \approx 46 \left[ \frac{T_e}{1 \text{ MK}} \right] [\text{Mm}] \quad (4)$$

where  $k_b$  is the Boltzmann constant,  $T_e$  is electron temperature,  $\mu$  is mean molecular weight ( $\approx 1.4$  for the solar corona),  $m_H$  is mass of the hydrogen atom, and  $g$  is acceleration due to gravity at the solar surface (see e.g., Aschwanden et al. 1999).

Moreover, observationally measured quantity such as intensity of an optically thin emission line depends on electron number density, i.e.  $I \propto N_e^\beta$  where  $1 < \beta < 3$ , and value of  $\beta$  depends upon whether the given line is allowed, forbidden, or inter-system (Mason & Monsignori Fossi 1994). In this study, we have chosen only allowed lines to do the line width analysis. Some density sensitive forbidden lines were also chosen to calculate electron number density (see Table 1). In Figure 5, we plot variation of intensity obtained from all the spectral lines with height along AR1, AR2, and QS stripes.

Since dataset covers active and quiet Sun regions over wide range of wavelength, we identified several density sensitive line pairs formed over range of temperature. We selected Fe XI  $\lambda 182.167/\lambda 180.401$ , Si X  $\lambda 258.374/\lambda 261.056$ , Fe XII  $\lambda 196.640/\lambda 192.394$ , Fe XIII  $\lambda 196.525/\lambda 202.044$ , and Fe XIV  $\lambda 264.789/\lambda 274.204$  line pairs to obtain the electron number

density (Young et al. 2007). In order to perform density and temperature diagnostics on the active region loops, background subtraction plays an important role (e.g., Del Zanna & Mason 2003). O'Dwyer et al. (2011) analyzed the current dataset before and used quiet Sun region to study background emission. We follow the same strategy and use intensity along the quiet Sun stripes to perform background subtraction along active region stripes. Therefore, we use quiet Sun stripes BG and QS to subtract background emission from active region stripes AR1 and AR2 respectively (stripes are shown in Figure 3). All plasma diagnostics are performed over these background subtracted intensities.

In Figure 6, we plot variation of electron number density derived from selected spectral line pairs with height along AR1, AR2, and QS. Plots show that as height increases electron number density decreases, however, corresponding errorbar increases with height. Some of the lines in quiet Sun region show estimates with larger errorbars. Near the active region limb, electron number densities were estimated to be of the order of  $> 10^9 \text{ cm}^{-3}$  which drops to around  $10^8 \text{ cm}^{-3}$  in the far off-limb region. Densities obtained from Fe XI, and Fe XII line pairs show almost similar numbers, whereas those obtained from Fe XIII, and Si X line pairs show similar values. Near the limb region, densities from Fe XI, and Fe XII pairs show consistently larger values than that of Fe XIII, and Si X pairs. However, they all seem to converge towards similar values beyond the distance of 80 Mm ( $< 5 \times 10^8 \text{ cm}^{-3}$ ) and 95 Mm ( $< 4.5 \times 10^8 \text{ cm}^{-3}$ ) along AR1 and AR2 respectively. Densities estimated from Fe XIV line pair are smaller in number as compared to other pairs and also falls-off more rapidly with height in both AR1 and AR2.

In the quiet Sun region, we found number densities to be

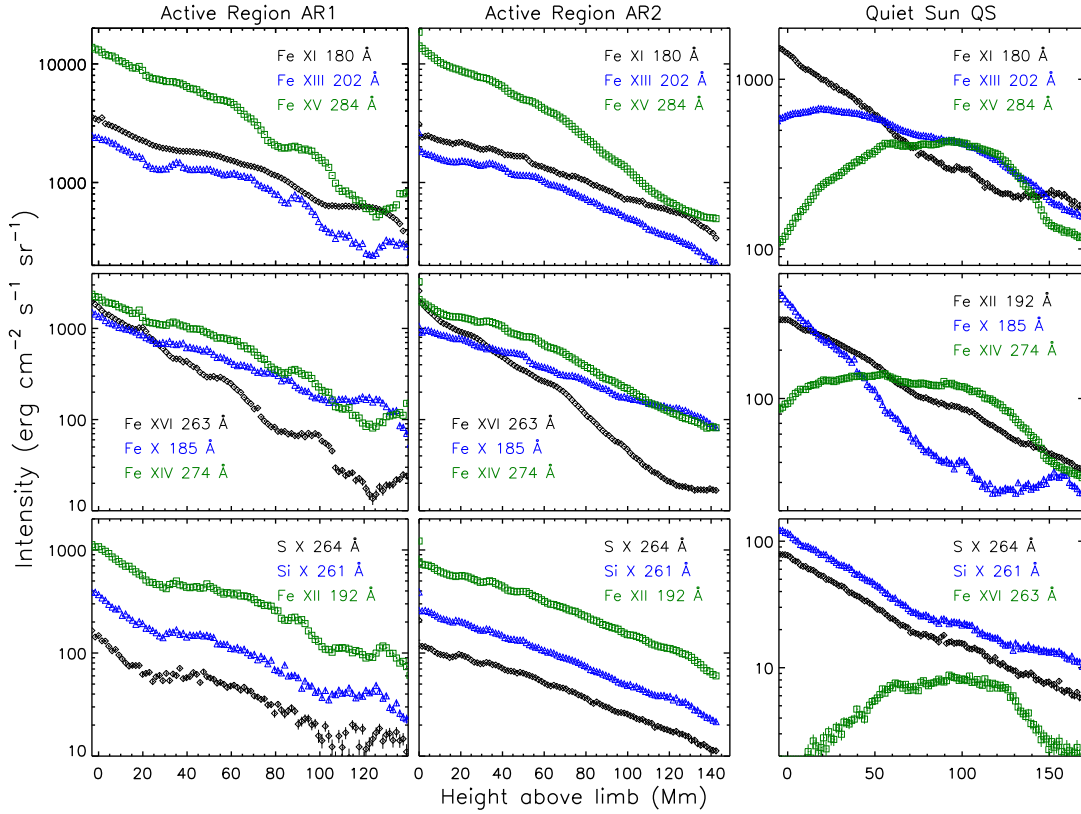


**Figure 5.** Intensity variation with height along active region AR1, AR2, and quiet Sun QS obtained from various spectral lines as labeled. True errors will also include 22% uncertainty of the observed intensity based on the pre-flight calibration of EIS (Lang et al. 2006).

lower than those in active region. In this case, densities estimated from Fe XII, and Fe XIII line pairs converge to similar numbers beyond 45 Mm ( $< 1.6 \times 10^8 \text{ cm}^{-3}$ ). However, near the limb, densities obtained from Fe XII pair are higher than that from Fe XIII pair. Densities obtained from Si X pair are higher than that estimated from Fe XII, and Fe XIII pairs. Densities estimated from Fe XI and Fe XIV pairs near the limb are comparatively higher than those obtained from other line pairs but drops-off very rapidly with height.

We fitted electron number density variation with height along AR1, AR2, and QS with exponential function  $N_e = N_0 \exp(-h/H_d) + c$  using MPFIT routines (Markwardt 2009). Fits provide density scale heights  $H_d$  at different temperatures obtained from different spectral line pairs (see Table 2). Expected electron density scale heights  $\lambda(T_e)$  as per hydrostatic equilibrium model at different temperatures (see Equation 4) are also provided in the table. Comparison between two density scale heights indicate that both the active and quiet Sun regions are basically underdense with few exceptions from quiet Sun region.

As active region and quiet Sun stripes were observed over a range of temperature, we employed emission measure (EM) loci technique to examine the thermal structure of different stripes as a function of off-limb height. Several EM loci plots were constructed at different heights along the active region AR1, AR2, and quiet Sun QS stripes. In Figure 7, we present sample EM loci plots obtained at the height of 55 Mm above the off-limb. From the plots, it is clear that plasma along the line-of-sight is not isothermal at that height. Based on EM loci plots, distribution of plasma along all the stripes were found to be multi-thermal at all the heights. These results are in good agreement with the findings of O'Dwyer et al. (2011)

who analyzed the same dataset before. They found plasma in the active region to be multi-thermal at different distances from the limb. Similarly, Warren et al. (2008) also studied isolated coronal loops from the same active region when observed on-disk and found them to be not isothermal. Thus, based on current and previous studies, plasma along the different active region stripes can be considered as multi-thermal. This may indicate that emission in different lines are coming from either single coronal structure formed over wide range of temperature or there exist multiple structures at different temperatures along the line-of-sight. Moreover, plasma along the off-limb quiet Sun region appears to be nearly isothermal if the contributions from hot lines are excluded. Figure 5 shows that intensities obtained from hot lines along QS are increasing with height near off-limb regions. This may suggest some possible contaminations in the hot lines from nearby active region.

### 3.2. Non-thermal Velocity

Non-thermal velocities are an important ingredient for calculation of Alfvén wave energy flux. These have been extracted from the observed emission line profiles as follows. Observed full width half maximum (FWHM) of any coronal spectral line is given by,

$$FWHM = \left[ 4 \ln 2 \left( \frac{\lambda}{c} \right)^2 \left( \frac{2k_b T_i}{M_i} + \xi^2 \right) + W_{inst}^2 \right]^{1/2} \quad (5)$$

where  $T_i$  is ion temperature,  $M_i$  ion mass,  $\xi$  is non-thermal velocity, and  $W_{inst}$  is the instrumental width. EIS/Hinode instrumental width is not constant, and is found to vary with

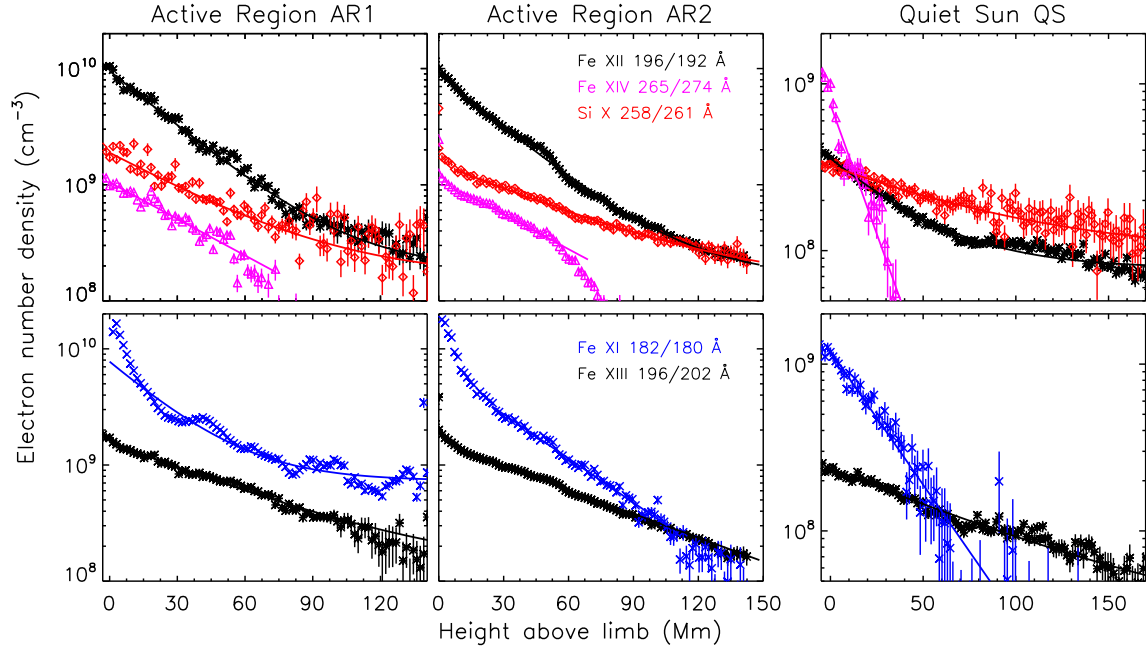


**Figure 6.** Electron number density variation with height along active region AR1, AR2, and quiet Sun QS obtained from different density sensitive spectral line pairs as labeled. Over-plotted continuous lines represent fitted exponential decay profile to obtain density scale heights from various spectral line pairs (see also Table 2).

**Table 2**  
Electron number density scale heights obtained from various spectral line pairs along active region AR1, AR2, and quiet Sun QS.

Ion	Wavelength (Å)	$T_{peak}$ (MK)	Hydrostatic height (Mm)	Density scale height (Mm)		
				AR1	AR2	QS
Fe XI	182.167/180.401	1.37	63.02	$24.86 \pm 0.31$	$34.22 \pm 0.26$	$27.13 \pm 0.98$
Si X	258.374/261.056	1.41	64.98	$39.84 \pm 2.15$	$53.61 \pm 2.25$	$78.12 \pm 9.91$
Fe XII	196.640/192.394	1.58	72.91	$26.98 \pm 0.36$	$28.54 \pm 0.20$	$38.70 \pm 0.66$
Fe XIII	196.525/202.044	1.78	81.80	$55.23 \pm 1.44$	$63.44 \pm 0.22$	$90.61 \pm 5.48$
Fe XIV	264.789/274.204	2.00	91.78	$41.37 \pm 0.56$	$43.53 \pm 0.32$	$14.00 \pm 0.96$

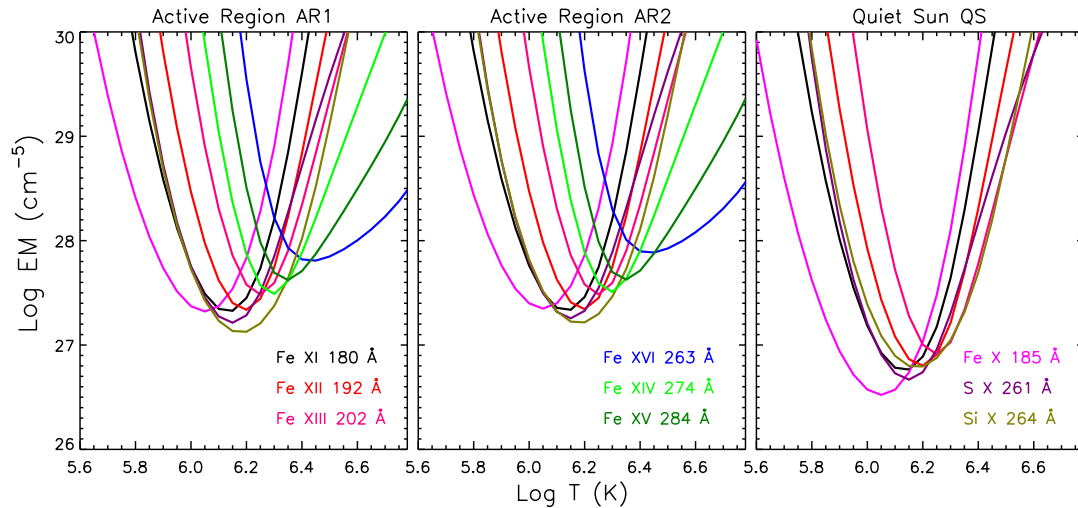


**Figure 7.** EM loci plots obtained at off-limb height of 55 Mm along AR1, AR2, and QS.

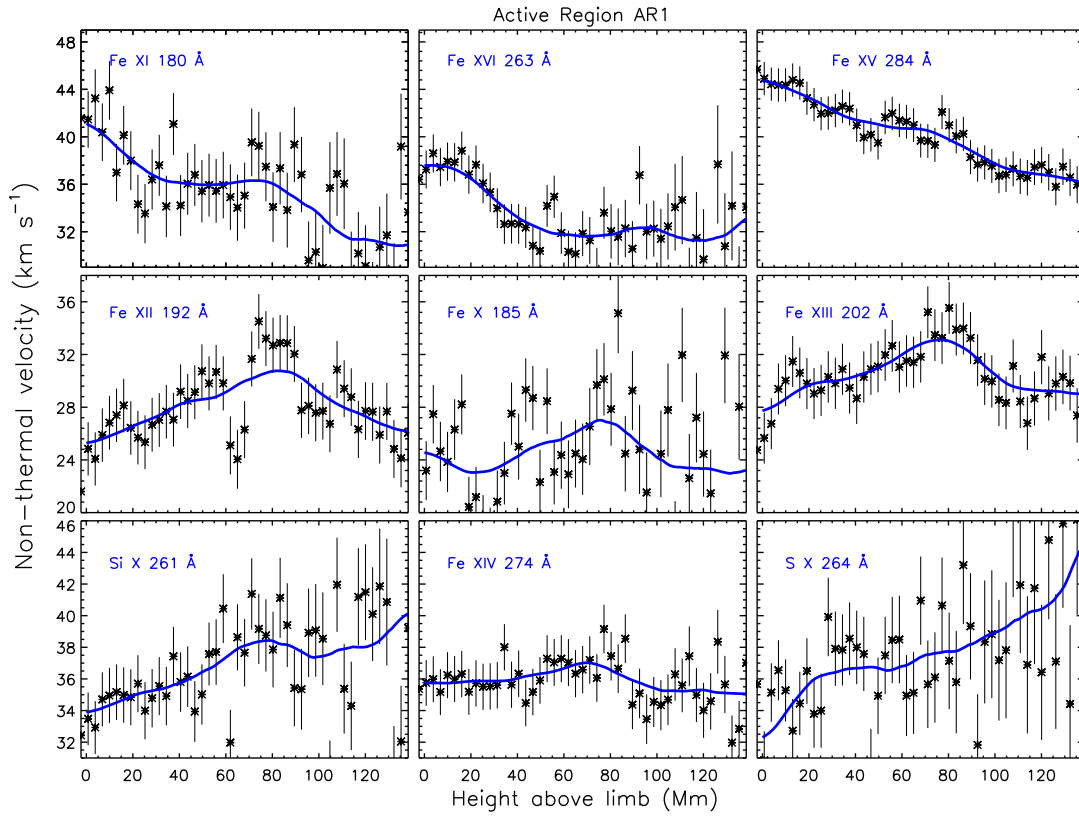


**Figure 8.** Variation of non-thermal velocity with height along active region AR1 obtained from various spectral lines as labeled. Overplotted continuous lines in all the panels show smooth variation of data-points obtained using 20-point running average.

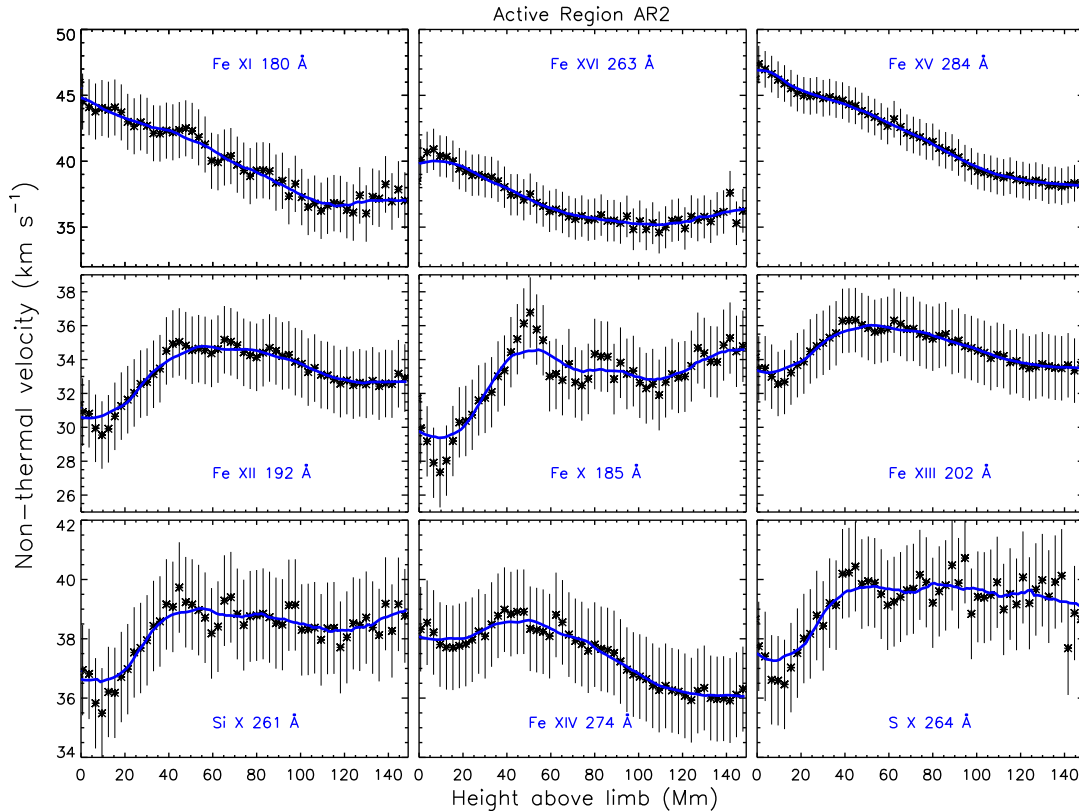


**Figure 9.** Same as Figure 8 but for active region AR2.



CCD Y-pixel position along the slit<sup>5</sup>. EIS instrumental width for 2'' slit varies between 64–74 mÅ for a downloaded central 512-pixels (starting from pixels 256 to 767). These widths were calculated using IDL routine EIS\_SLIT\_WIDTH provided by EIS team. Instrumental widths were then subtracted from the FWHM of spectral lines accordingly. We further calculated non-thermal components by subtracting thermal components from each spectral lines. Thermal components were calculated after assuming ion temperatures to be equal to the peak formation temperature of spectral lines as found from contribution functions (see Figure 2 and Table 1). After subtraction of instrumental width, line widths were primarily dominated by non-thermal components. Errorbars on non-thermal velocities were calculated using errors in the profile fitting, 3 mÅ error in instrumental width, and errors in assumed thermal temperatures which were taken to be half width half maxima (HWHM) of Gaussian fits applied to contribution functions of respective spectral lines.

In Figures 8, 9, and 10, we plot non-thermal velocities ( $\xi$ ) obtained from various spectral lines with height along active regions AR1, AR2, and quiet Sun QS respectively. We also over-plot 20-point running average of data-points to visualize variations on longer spatial scale. Non-thermal velocities obtained from warm lines such as Fe x 185 Å, Fe xii 192 Å, and Fe xiii 202 Å show initial increase from  $\approx 24$  km s<sup>-1</sup> near the limb to  $\approx 33$  km s<sup>-1</sup> at around height of 80 Mm, whereas those obtained from Si x 261 Å, and S x 264 Å show increase from  $\approx 34$  km s<sup>-1</sup> to  $\approx 39$  km s<sup>-1</sup> at the similar heights along AR1. Beyond these heights, non-thermal velocities either decrease or remain almost constant with some scattered data-points.

Variation of non-thermal velocities with height along AR2 also show similar pattern as in AR1 but their values are enhanced by  $\approx 2 - 3$  km s<sup>-1</sup>. This possible enhancement along AR2 could be due to integration taken over larger spatial scale to deduce the non-thermal velocities. On comparison with polar regions (e.g., Banerjee et al. 2009; Bemporad & Abbo 2012), non-thermal velocities obtained from Fe xii line in the active regions are consistently smaller in magnitude but shows sharp increase with height. However, recent findings of Lee et al. (2014) showed consistent decrease in non-thermal velocities along the cool loop and dark lane in the off-limb active region. Moreover, non-thermal velocities obtained from hot lines such as Fe xv 284 Å, and Fe xvi 263 Å show gradual decrease with height. Velocities obtained from hot Fe xv 284 Å line shows decrease from  $\approx 45$  km s<sup>-1</sup> near the limb to  $\approx 36$  km s<sup>-1</sup> beyond 100 Mm along AR1, whereas Fe xvi 263 Å line shows decrease from  $\approx 38$  km s<sup>-1</sup> to  $\approx 32$  km s<sup>-1</sup>. Variations obtained from hot Fe xv 284 Å, and Fe xvi 263 Å lines along AR2 show pattern again similar to that in AR1 with velocities being again enhanced by  $\approx 2 - 3$  km s<sup>-1</sup>. Surprisingly, warm Fe xi 180 Å line shows pattern similar to that of hot lines whereas Fe xiv 274 Å line shows intermediate behavior of hot and warm lines. Singh et al. (2006) performed line width study along steady coronal structures using data from Norikura coronagraph. They found decrease in FWHM of hot Fe xiv 5303 Å line up to the distance of 300'' above the limb which became constant thereafter. They also found increase in FWHM of warm Fe x 6374 Å line up to the distance of 250'' which remained unchanged further. FWHM of intermediate lines (Fe xi 7892 Å and Fe xiii 10747 Å) showed intermediate

behavior. Thus, results of line width variation with height do indicate some temperature dependence. Findings in this study are almost similar to those of Singh et al. (2006) with some shift in temperature dependence. This shift might be specific to the active regions studied. However, cause for exceptional behavior of warm Fe xi 180 Å line in this study is unknown and can not be speculated at this stage. Recently, Brooks & Warren (2016) surveyed 15 non-flaring on-disk active regions using EIS/Hinode. They measured non-thermal velocities at specific locations in the cores of solar active regions over the temperature range of 1–4 MK. However, they did not find any significant trend with temperature.

In the quiet Sun region, non-thermal velocities obtained from warm iron lines show consistent decrease with height. Non-thermal velocities obtained from warm Si x and S x lines show almost constant value of  $\approx 34$  km s<sup>-1</sup> and  $\approx 36$  km s<sup>-1</sup> respectively with height, however, they do show some large scatter around. Non-thermal velocities obtained from hot Fe xiv and Fe xv lines also show decrease with height similar to warm lines. No visible pattern can be inferred from hot Fe xvi line as signal in this line in the quiet Sun region is mostly due to scattered light as mentioned earlier. These finding are similar to those of Harrison et al. (2002) where they studied spectral line profiles of warm Mg x 625 Å line from quiet clean corona. They found narrowing of emission lines as a function of height similar to findings in the current study. They attributed narrowing of profiles with height to dissipation of wave activity.

### 3.3. Alfvén wave energy flux

Alfvén wave energy flux can be calculated by using Equation 2. In a flux tube geometry,  $B \times A$  will always be a constant. Because in a constant magnetic field model, cross-sectional area will remain constant, thus, product will also remain constant. However, in the case of expanding flux tube model,  $B$  will decrease with height (let us assume inverse square field dependence), whereas  $A$  will increase with squared radius dependence, thus, product of  $B$  and  $A$  will again be constant (see Moran 2001). Therefore, total Alfvén wave energy flux will always be proportional to  $\sqrt{N_e} \xi^2$  in either case. Henceforth, if total Alfvén wave energy flux is conserved as waves propagates outward,  $\sqrt{N_e} \xi^2$  will remain constant with height. In Figures 11, 12, and 13, we plot variations of  $\sqrt{N_e} \xi^2$  with height obtained from selected spectral lines along active region AR1, AR2, and quiet Sun QS respectively. As electron number densities were estimated only from few spectral line pairs, therefore for rest of the lines, we choose number densities obtained from line pairs formed at nearest temperature. Plots clearly show that product  $\sqrt{N_e} \xi^2$  decreases with height in all spectral lines in all the regions. This provides clear evidence of damping of Alfvén wave energy flux with height in the both off-limb active and quiet Sun region. Alfvén wave energy fluxes are found to be  $\approx 1.85 \times 10^7$  erg cm<sup>-2</sup> s<sup>-1</sup> near the limb which decreases to  $\approx 0.86 \times 10^7$  erg cm<sup>-2</sup> s<sup>-1</sup> at around height of 70 Mm as calculated from Fe xii 192 Å spectral line. To calculate the Alfvén wave energy flux, we assumed coronal magnetic field strength of 39 G as measured by Van Doorselaere et al. (2008) using loop oscillations. Calculated Alfvén wave energy fluxes are of similar order of magnitude which is required to maintain the active region corona ( $\approx 10^7$  erg cm<sup>-2</sup> s<sup>-1</sup> as estimated by Withbroe & Noyes 1977). Moreover, coronal magnetic field strength can vary like 10 G and 35 G as measured by Lin et al. (2000) in two active regions

<sup>5</sup> [http://sohoftp.nascom.nasa.gov/solarsoft/hinode/eis/doc/eis\\_notes/07\\_LINE\\_WIDTH/eis\\_swnote\\_07.pdf](http://sohoftp.nascom.nasa.gov/solarsoft/hinode/eis/doc/eis_notes/07_LINE_WIDTH/eis_swnote_07.pdf)

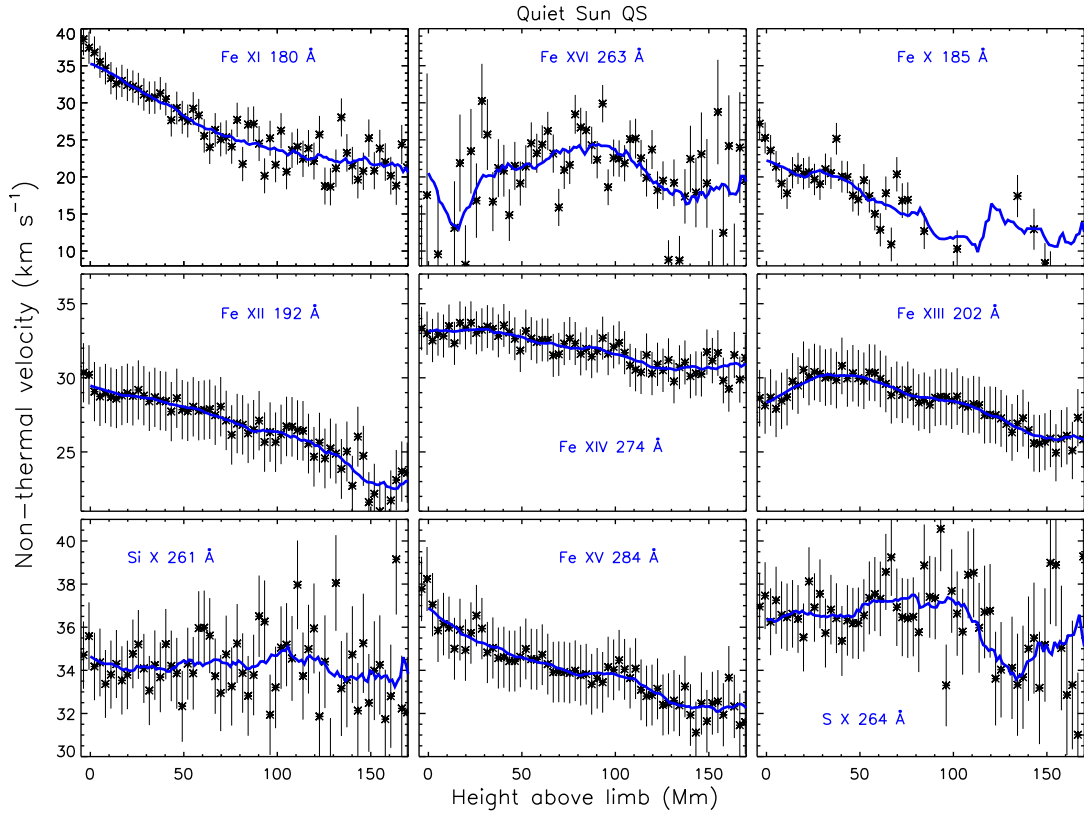


**Figure 10.** Same as Figure 8 but for quiet Sun QS.

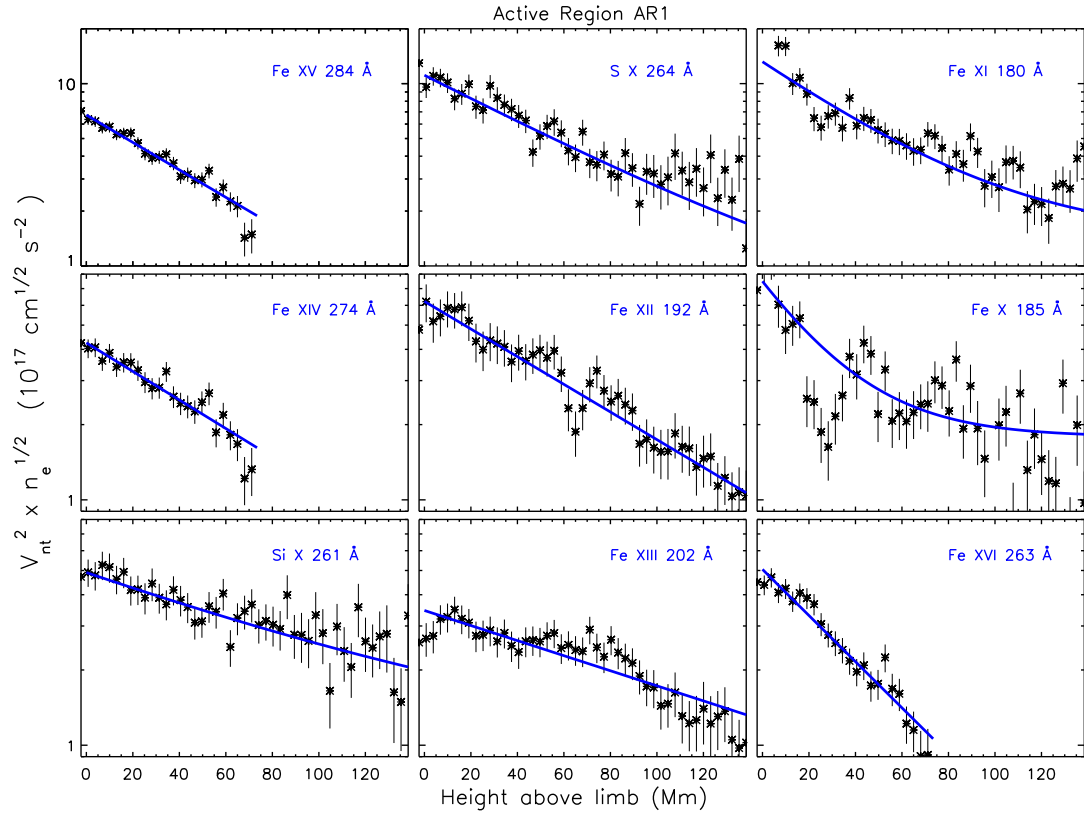


**Figure 11.** Variation of proportional Alfvén wave energy flux ( $\sqrt{N_e} \xi^2$ ) with height along active region AR1 obtained from various spectral lines as labeled. Over-plotted continuous lines are fitted exponential decay profile to obtain wave damping lengths from various spectral lines formed at range of temperature (see also Table 3).

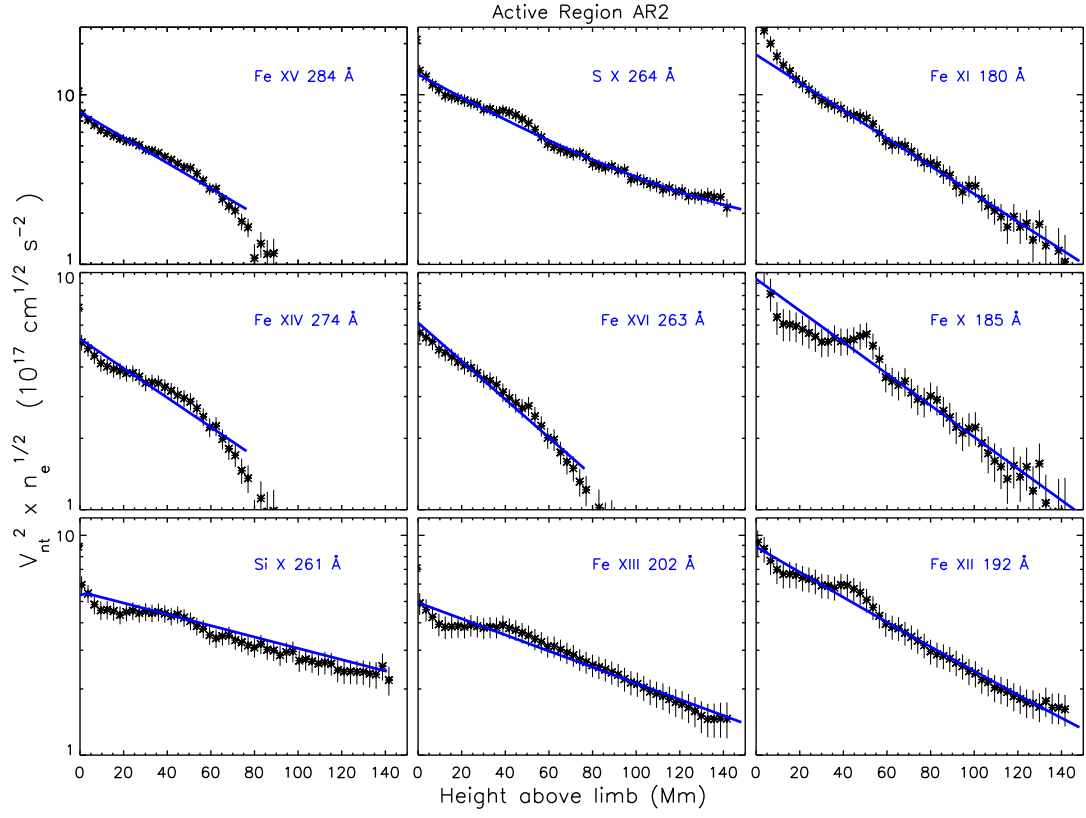


Figure 12. Same as Figure 11 but for active region AR2.

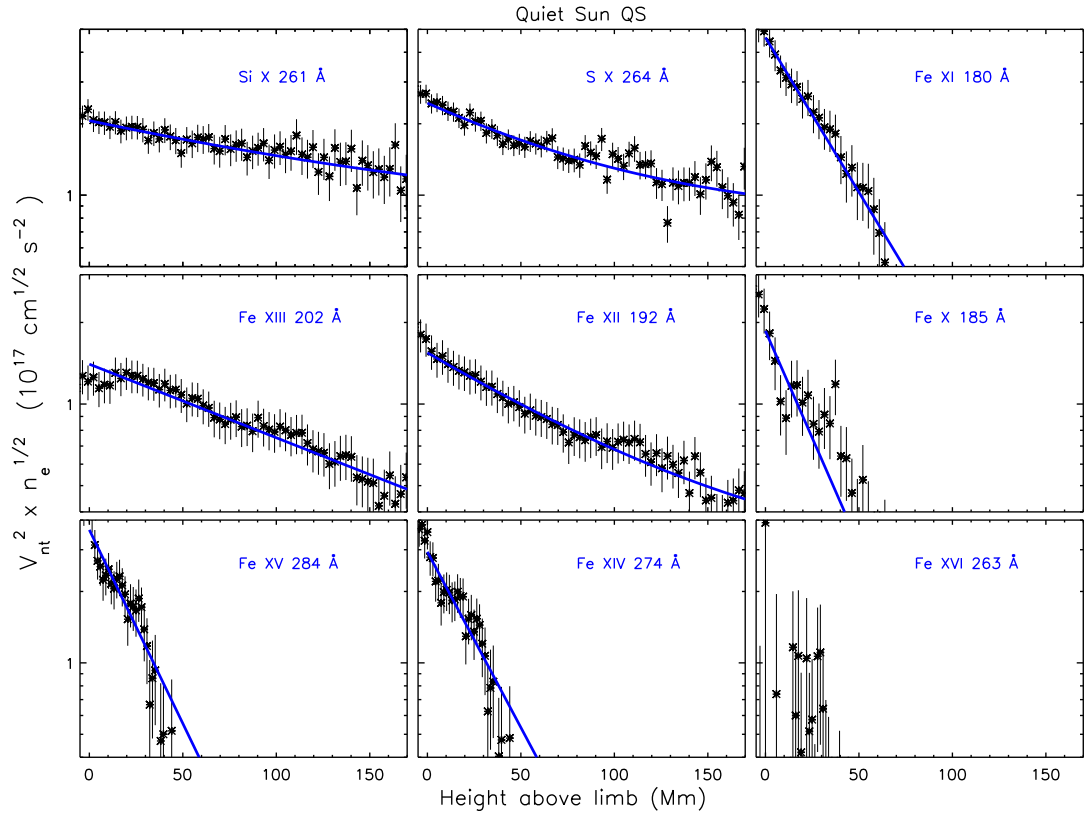


Figure 13. Same as Figure 11 but for quiet Sun QS.

**Table 3**  
Damping lengths derived from various spectral lines along active region AR1, AR2, and quiet Sun QS.

Ion	Wavelength (Å)	$T_{peak}$ (MK)	Damping length $D_l$ (Mm)		
			AR1	AR2	QS
Fe x	184.537	1.12	28.31 ± 6.72	65.19 ± 3.45	27.54 ± 2.39
Fe xi	180.401	1.37	46.52 ± 7.62	52.93 ± 0.82	33.29 ± 2.44
Si x	261.056	1.41	114.87 ± 77.31	161.69 ± 11.01	169.95 ± 181.20
S x	264.231	1.55	65.02 ± 12.47	56.32 ± 5.72	84.47 ± 23.77
Fe xii	192.394	1.58	78.49 ± 4.38	73.70 ± 13.44	91.95 ± 20.12
Fe xiii	202.044	1.78	144.1 ± 12.44	118.30 ± 6.85	159.98 ± 10.49
Fe xiv	274.204	2.00	75.99 ± 6.00	70.06 ± 4.45	29.31 ± 3.50
Fe xv	284.163	2.24	57.68 ± 2.97	57.99 ± 2.66	26.59 ± 2.79
Fe xvi	262.976	2.82	47.05 ± 2.65	53.85 ± 2.90	---

at distances of 0.12 and 0.15  $R_{\odot}$  using longitudinal Zeeman effect in Fe xiii 10747 Å spectral line. Therefore, if assumed magnetic field strength is of the order of 10 G, then Alfvén wave energy fluxes will be slightly less than the energy flux required to maintain the corona. One thing to be noted here that although Alfvén waves are getting gradually damped with height, non-thermal velocities obtained from warm spectral lines were initially increasing with height in the active region. This indicates that damping of Alfvén waves can only be inferred from complete calculation of total Alfvén wave energy flux with height. Only non-thermal velocity estimates with height will not serve the purpose.

Upon finding the evidence of damping of Alfvén wave energy flux with height, we further obtain damping length in all the spectral lines covering range of temperature. Effect of damping can be calculated by multiplying  $e^{-h/D_l}$  to the proportional Alfvén wave energy flux  $\sqrt{N_e} \xi^2$ , where  $D_l$  is termed as ‘damping length’ for total Alfvén wave energy flux,

$$F_{wt} \propto \sqrt{N_e} \xi^2 e^{-h/D_l} \quad (6)$$

$$F_{wt} \approx A \sqrt{N_e} \xi^2 e^{-h/D_l} + B \quad (7)$$

where A and B are appropriate constants. Henceforth, we obtained damping length by fitting the  $F_{wt}$  values in different spectral lines as per Equation 7 using MPFIT routines (Markwardt 2009). Derived damping lengths  $D_l$  from various spectral lines along active region AR1, AR2, and quiet Sun QS are in the range of 25-170 Mm and provided in the Table 3. Bemporad & Abbo (2012) also reported decay of Alfvén wave energy flux with height in the polar coronal hole region. However, they performed linear fit to decay profile and estimated decay rates to be  $-1.07 \times 10^{-3}$  erg cm $^{-1}$  below 0.03  $R_{\odot}$  and  $-4.5 \times 10^{-5}$  erg cm $^{-1}$  between 0.03-0.4  $R_{\odot}$ . Equivalent damping length for the decay rate between 0.03-0.4  $R_{\odot}$  is calculated to be around 95 Mm. They performed measurements using EIS Fe xii 195 Å spectral line. In this work, damping lengths obtained from Fe xii 192 Å lines are in the range of 75–90 Mm in both active and quiet Sun regions. This suggests that damping lengths obtained from both the studies are comparable.

#### 4. DISCUSSIONS

In this work, we found clear evidence of damping of Alfvén waves in the off-limb active and quiet Sun region. Damping lengths were found to be different for different spectral lines formed at different temperatures (see Table 3). We further explore existence of any temperature dependence on various

decay lengths obtained in this study. Henceforth, we analyze density scale heights and Alfvén wave damping lengths with peak formation temperature of their respective spectral lines (see Table 1). We plot density scale heights obtained from the different line pairs with respect to their peak formation temperature (see top panels of Figure 14). Density scale heights first increase and later decrease with temperature. However, density scale height obtained from Fe xii pair does not follow this trend. Moreover, hydrostatic scale heights as expected from Equation 4 are also provided in Table 2. As mentioned earlier, comparison between the two density scale heights indicate that both active and quiet Sun regions are basically underdense, with few exceptions from quiet Sun region. However, it appears that emissions coming from spectral lines formed near the temperature of 1.8 MK are more closer to be in hydrostatic equilibrium than those formed different from 1.8 MK in the active region. This may be speculated as observed region to be filled with plasma of temperature nearly 1.8 MK and has poor supply for other cooler and hotter plasma. This result might be a characteristic of observed active region, and different active regions might have different temperature distribution.

In the bottom panels of Figure 14, we plot damping lengths obtained from different spectral lines with respect to their peak formation temperature. Different panels show that damping lengths first increase and later decrease with temperature. Maximum damping length is attained at around temperature of 1.78 MK (corresponds to Fe xiii 202 Å) for all the active region and quiet Sun stripes. We would also like to point out that several structures were traced and analyzed as mentioned earlier. Although obtained decay lengths were not same, results followed similar pattern for all the analyzed structures. Henceforth, obtained results indicate measurement of different damping lengths for different temperatures. These results can either be interpreted as temperature dependent damping of Alfvén waves or measurement of different damping lengths in different coronal structures formed over wide range of temperature along the our line-of-sight.

Possible temperature dependent damping length of Alfvén waves may indicate that thermal conduction plays some important role in the damping of these waves. However, role of thermal conduction in the damping of Alfvén waves is not much explored (e.g., Van Ballegooijen et al. 2011). Although it is very well studied for the case of slow magneto-acoustic waves (e.g., De Moortel et al. 2002). Role of thermal conduction in the damping of slow magneto-acoustic waves were recently observed by Gupta (2014) and Krishna Prasad et al. (2014) based on possible period (of waves) dependent damping length. In this study, although we do not have any infor-

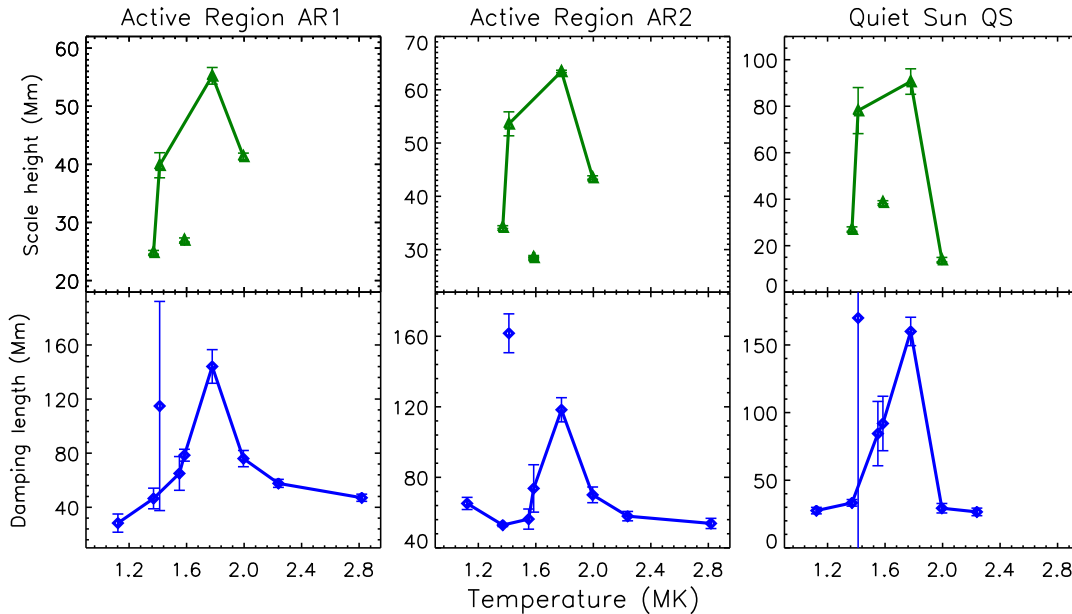


**Figure 14.** Variation of density scale heights (top panels) and Alfvén waves damping lengths (bottom panels) obtained from different spectral lines with respect to their peak formation temperature.

mation on wave period, we have coverage over wide range of temperature. Work of [De Moortel et al. \(2002\)](#) suggested that slightly enhanced thermal conductivity may explain observed damping lengths of 40–50 Mm for slow waves. These enhancements in thermal conductivity were later also suggested by [Gupta \(2014\)](#). In this study, observed damping lengths for Alfvén waves are in the range of 25–170 Mm as obtained from different temperature lines. Henceforth, these results demand for detailed investigation of role of thermal conduction in the damping of Alfvén waves.

Slow magneto-acoustic waves in the solar corona propagate along the field lines with propagation speed of the order of  $100 \text{ km s}^{-1}$  and velocity amplitude of the order of  $5\text{--}10 \text{ km s}^{-1}$ . Active region studied in this work is located near the limb and derived results are mainly focused on off-limb regions. In the off-limb region, magnetic field lines are generally found to be oriented nearly perpendicular to the observers line-of-sight. Therefore, contribution from observed Doppler velocities due to propagation of slow magneto-acoustic waves in the measurement of non-thermal velocities will be minimal. Similarly, studies on measurement of plasma flows in the active region loops indicate temperature dependent flow speeds. [Del Zanna \(2008\)](#) and [Tripathi et al. \(2009\)](#) measured absolute flow speeds to be less than  $30 \text{ km s}^{-1}$  along the active region loops using similar spectral lines formed over temperature range of  $0.6\text{--}2 \text{ MK}$ . They found decrease in flow speeds with increase in temperature (redshift to blueshift). Moreover, [Brooks & Warren \(2011\)](#) also measured on an average Doppler velocity of  $-22 \text{ km s}^{-1}$  from the edges of active regions. Generally loops cross an active region in the East-West direction, so flows along the off-limb loops will either be directed toward or away from the observers line-of-sight (if loops are not radially directed). This may lead to some enhancements in the line-width. However, as velocities in line-width measurements add in quadrature, contribution of Doppler velocities due to plasma upflows ( $< 10 \text{ km s}^{-1}$ , due to inclination of loops along the line-of-sight) will again be minimal in the non-thermal velocities. Moreover, there might be some enhancement in the non-thermal broad-

ening due to these factors but given the range of errorbars ( $2\text{--}4 \text{ km s}^{-1}$ ), their contribution can not be quantified. Measurements on AR2 which were obtained after taking average over larger spatial length, shows enhancements in non-thermal velocities by  $\approx 2\text{--}3 \text{ km s}^{-1}$  as compared to measurements on AR1. This could possibly be the effect of different Doppler shifted flows present along several different loop structures which were summed together to obtain the integrated profile, and thus, resulted in larger non-thermal velocities. Henceforth, measured non-thermal velocities along AR2 can only be considered as an upper limit.

As mentioned earlier, role of thermal conduction in the damping of slow magneto-acoustic waves is well known. One of the possibility of damping of Alfvén waves would be that Alfvén wave energy is being transferred to slow magneto-acoustic waves. These slow waves will further get easily dissipated via thermal conduction and will finally show up as temperature dependent damping of Alfvén waves. [Zaqarashvili et al. \(2006\)](#) studied wave energy conversion process in the non-linear ideal MHD framework. They demonstrated that wave energy can be converted from Alfvén waves to slow magneto-acoustic waves near the region of corona where plasma- $\beta$  approaches unity. As contributions from slow magneto-acoustic waves in the current measurements of non-thermal velocities are minimal, henceforth, only the damping of Alfvén waves can be inferred from the observed non-thermal velocities.

## 5. SUMMARY AND CONCLUSIONS

We investigated off-limb active and quiet Sun region using spectroscopic data from EIS/Hinode. We studied height dependence of basic plasma parameters such as intensity, electron number density, and non-thermal velocity along the active region and quiet Sun. These estimated parameters enabled us to further study height dependence of Alfvén wave energy flux in the both regions. Main findings of our analysis are summarized as,

- We identified several isolated spectral lines with good signal to noise ratio in the off-limb regions. These lines

are formed at different temperatures and cover the temperature range of 1.1–2.8 MK.

- We obtained electron densities and corresponding scale heights from different spectral line pairs which suggested that observed active and quiet Sun regions are basically underdense with few measured exceptions from quiet Sun region.
- Non-thermal velocities measured from warm spectral lines first showed increase with height and later showed either decrease or almost constant value with height in the far off-limb active region whereas hot lines showed gradual decrease with height. However, those measured from various spectral lines in the quiet Sun region showed either gradual decrease or almost constant value with height.
- Calculated Alfvén wave energy fluxes were similar to or slightly less than the energy required to maintain the active region corona. Results also showed damping of Alfvén wave energy flux with height.
- We found damping lengths of Alfvén wave energy flux ( $D_I$ ) to be in the range of 25–170 Mm as measured from different spectral lines formed at different temperatures.
- Variation of damping lengths first showed increase and later decrease with increasing temperature. Damping length peaked at around temperature of 1.78 MK in the both active and quiet Sun regions.

This work provides measurements of non-thermal velocities and Alfvén wave energy fluxes at wide range of temperature. Possible interpretation of these results would be either temperature dependent damping of Alfvén waves or measurements along different coronal structures formed at different temperatures. Possible temperature dependent damping may suggest some important role of thermal conduction in the damping of Alfvén waves in the lower corona. This may even suggest some non-linear coupling between Alfvén and slow MHD modes (see [Zaqarashvili et al. 2006](#)). We believe this to be an important result as this will provide more insight in to the dissipation mechanism of Alfvén waves. Recent 3-D MHD models of [Van Ballegoijen et al. \(2011\)](#) explained role of Alfvén wave turbulence in the heating of solar chromosphere and corona. They predicted velocity amplitude of Alfvén waves in the corona to be in the range of 20–40 km s<sup>-1</sup> so as to maintain the typical active region loops. In our analysis, we found almost similar wave velocity amplitude in the active region. Observed damping rate of Alfvén wave energy flux with height is similar or slightly less than to the requirements of coronal active region. [Asgari-Targhi et al. \(2014\)](#) also measured non-thermal velocities in the range of 25–45 km s<sup>-1</sup> using observation from EIS/Hinode along the on-disk individual coronal loop length. Their findings were consistent with the predictions from Alfvén wave turbulence model. However, we would also like to point out that model of [Van Ballegoijen et al. \(2011\)](#) still do not include effects of thermal conduction and radiative losses. Therefore, at present, exact form of any relation between damping length of Alfvén wave turbulence and temperature can not be comprehended. Henceforth, these results demand for development of more sophisticated 3-D MHD models of Alfvén wave propagation and dissipation including the effects of thermal conduction

and non-linear coupling between various MHD modes in the solar atmosphere.

Author thanks the referee for the careful reading and constructive criticism that helped improve the paper. GRG is supported through the INSPIRE Faculty Award of Department of Science and Technology (DST), India. Author thanks T. V. Zaqarashvili for the helpful discussion and P. Young for helpful clarifications. Hinode is a Japanese mission developed and launched by ISAS/JAXA, collaborating with NAOJ as a domestic partner, NASA and STFC (UK) as international partners. Scientific operation of the Hinode mission is conducted by the Hinode science team organized at ISAS/JAXA. This team mainly consists of scientists from institutes in the partner countries. Support for the post-launch operation is provided by JAXA and NAOJ (Japan), STFC (U.K.), NASA (U.S.A.), ESA, and NSC (Norway).

## REFERENCES

- Alfvén, H. 1942, *Nature*, 150, 405  
 —. 1947, *MNRAS*, 107, 211  
 Arregui, I. 2015, *Philosophical Transactions of the Royal Society of London Series A*, 373, 40261  
 Aschwanden, M. J., Newmark, J. S., Delaboudinière, J., et al. 1999, *ApJ*, 515, 842  
 Asgari-Targhi, M., van Ballegoijen, A. A., & Imada, S. 2014, *ApJ*, 786, 28  
 Banerjee, D., Gupta, G. R., & Teriaca, L. 2011, *Space Sci. Rev.*, 158, 267  
 Banerjee, D., Pérez-Suárez, D., & Doyle, J. G. 2009, *A&A*, 501, L15  
 Banerjee, D., Teriaca, L., Doyle, J. G., & Wilhelm, K. 1998, *A&A*, 339, 208  
 Bemporad, A., & Abbo, L. 2012, *ApJ*, 751, 110  
 Brooks, D. H., & Warren, H. P. 2011, *ApJL*, 727, L13  
 —. 2016, *ApJ*, 820, 63  
 Cranmer, S. R., Asgari-Targhi, M., Miralles, M. P., et al. 2015, *Philosophical Transactions of the Royal Society of London Series A*, 373, 40148  
 Cranmer, S. R., & van Ballegoijen, A. A. 2005, *ApJS*, 156, 265  
 Cranmer, S. R., van Ballegoijen, A. A., & Edgar, R. J. 2007, *ApJS*, 171, 520  
 Culhane, J. L., Harra, L. K., James, A. M., et al. 2007, *Sol. Phys.*, 243, 19  
 De Moortel, I., & Browning, P. 2015, *Philosophical Transactions of the Royal Society of London Series A*, 373, 40269  
 De Moortel, I., Hood, A. W., Ireland, J., & Walsh, R. W. 2002, *Sol. Phys.*, 209, 89  
 De Moortel, I., & Nakariakov, V. M. 2012, *Royal Society of London Philosophical Transactions Series A*, 370, 3193  
 Del Zanna, G. 2008, *A&A*, 481, L49  
 Del Zanna, G., Dere, K. P., Young, P. R., Landi, E., & Mason, H. E. 2015, *A&A*, 582, A56  
 Del Zanna, G., & Mason, H. E. 2003, *A&A*, 406, 1089  
 Dere, K. P., Landi, E., Mason, H. E., Monsignori Fossi, B. C., & Young, P. R. 1997, *A&AS*, 125, 149  
 Doyle, J. G., Banerjee, D., & Perez, M. E. 1998, *Sol. Phys.*, 181, 91  
 Freeland, S. L., & Handy, B. N. 1998, *Sol. Phys.*, 182, 497  
 Gupta, G. R. 2014, *A&A*, 568, A96  
 Gupta, G. R., Banerjee, D., Teriaca, L., Imada, S., & Solanki, S. 2010, *ApJ*, 718, 11  
 Gupta, G. R., Tripathi, D., & Mason, H. E. 2015, *ApJ*, 800, 140  
 Hahn, M., Landi, E., & Savin, D. W. 2012, *ApJ*, 753, 36  
 Hahn, M., & Savin, D. W. 2014, *ApJ*, 795, 111  
 Harrison, R. A., Hood, A. W., & Pike, C. D. 2002, *A&A*, 392, 319  
 Hassler, D. M., Rottman, G. J., Shoub, E. C., & Holzer, T. E. 1990, *ApJL*, 348, L77  
 Jess, D. B., Mathioudakis, M., Erdélyi, R., et al. 2009, *Science*, 323, 1582  
 Jess, D. B., Morton, R. J., Verth, G., et al. 2015, *Space Sci. Rev.*, 190, 103  
 Klimchuk, J. A. 2015, *Philosophical Transactions of the Royal Society of London Series A*, 373, 40256  
 Kosugi, T., Matsuzaki, K., Sakao, T., et al. 2007, *Sol. Phys.*, 243, 3  
 Krishna Prasad, S., Banerjee, D., & Van Doorsselaere, T. 2014, *ApJ*, 789, 118  
 Lang, J., Kent, B. J., Paustian, W., et al. 2006, *Appl. Opt.*, 45, 8689  
 Lee, K.-S., Imada, S., Moon, Y.-J., & Lee, J.-Y. 2014, *ApJ*, 780, 177  
 Lin, H., Penn, M. J., & Tomczyk, S. 2000, *ApJL*, 541, L83

- Markwardt, C. B. 2009, in *Astronomical Society of the Pacific Conference Series*, Vol. 411, *Astronomical Data Analysis Software and Systems XVIII*, ed. D. A. Bohlender, D. Durand, & P. Dowler, 251
- Mason, H. E., & Monsignori Fossi, B. C. 1994, *A&A Rev.*, 6, 123
- McIntosh, S. W., de Pontieu, B., Carlsson, M., et al. 2011, *Nature*, 475, 477
- Moran, T. G. 2001, *A&A*, 374, L9
- Morton, R. J., Tomczyk, S., & Pinto, R. 2015, *Nature Communications*, 6, 7813
- Morton, R. J., Verth, G., Hillier, A., & Erdélyi, R. 2014, *ApJ*, 784, 29
- O'Dwyer, B., Del Zanna, G., Mason, H. E., et al. 2011, *A&A*, 525, A137
- Parker, E. N. 1988, *ApJ*, 330, 474
- Parnell, C. E., & De Moortel, I. 2012, *Philosophical Transactions of the Royal Society of London Series A*, 370, 3217
- Singh, J., Sakurai, T., & Ichimoto, K. 2006, *ApJ*, 639, 475
- Suzuki, T. K., & Inutsuka, S. 2005, *ApJL*, 632, L49
- Testa, P., De Pontieu, B., & Hansteen, V. 2016, *ApJ*, 827, 99
- Tomczyk, S., McIntosh, S. W., Keil, S. L., et al. 2007, *Science*, 317, 1192
- Tripathi, D., Mason, H. E., Dwivedi, B. N., del Zanna, G., & Young, P. R. 2009, *ApJ*, 694, 1256
- Van Ballegoijen, A. A., Asgari-Targhi, M., Cranmer, S. R., & DeLuca, E. E. 2011, *ApJ*, 736, 3
- Van Doorselaere, T., Nakariakov, V. M., Young, P. R., & Verwichte, E. 2008, *A&A*, 487, L17
- Verdini, A., Velli, M., Matthaeus, W. H., Oughton, S., & Dmitruk, P. 2010, *ApJL*, 708, L116
- Warren, H. P., Ugarte-Urra, I., Doschek, G. A., Brooks, D. H., & Williams, D. R. 2008, *ApJL*, 686, L131
- Warren, H. P., Ugarte-Urra, I., & Landi, E. 2014, *ApJS*, 213, 11
- Withbroe, G. L., & Noyes, R. W. 1977, *ARA&A*, 15, 363
- Young, P. R., Del Zanna, G., Mason, H. E., et al. 2007, *PASJ*, 59, 857
- Zaqarashvili, T. V., Oliver, R., & Ballester, J. L. 2006, *A&A*, 456, L13